nature communications

Article

https://doi.org/10.1038/s41467-024-55515-0

Nano-seeding catalysts for high-density arrays of horizontally aligned carbon nanotubes with wafer-scale uniformity

Received: 2 April 2024

Accepted: 14 December 2024

Published online: 02 January 2025

Check for updates

Ying Xie[1,2,6], Yue Li[1,3,6], Zhisheng Peng[1,6], Chengyu Wang[4], Zanlin Qiu[1], Xinyi Cai[2], Tinglu Song[5], Jia Si[4], Xiaoxu Zhao[1], Liu Qian[1] ✉, Ziqiang Zhao[3] ✉ & Jin Zhang[1,2] ✉

In the realm of modern materials science, horizontally aligned carbon nanotube arrays stand as promising materials for the development of next-generation integrated circuits. However, their large-scale integration has been impeded by the constraints of current fabrication techniques, which struggle to achieve the necessary uniformity, density, and size control of carbon nanotube arrays. Overcoming this challenge necessitates a significant shift in fabrication approaches. Herein, we present a nano-seeding method that revolutionized the preparation of catalyst nanoparticles, crucial for carbon-nanotube-array synthesis. Our approach, underpinned by ion implantation and substrate processing, allows for precise control over catalyst formation. Further development of a vertical spraying chemical vapor deposition system homogenizes the gas flow and ensures the uniform growth of carbon nanotube arrays. This nano-seeding method culminates in the direct growth of one-inch carbon-nanotube-array wafers with the highest density of 140 tubes μm^{-1}. The high density and uniformity of the as-prepared carbon-nanotube-array wafers are validated through an advanced high-throughput characterization technique. The electrical properties of high on-state current, high on/off ratio and low subthreshold swing are demonstrated in field-effect transistors based on the arrays. This study propels the scalability of carbon-nanotube-array fabrication for future carbon-based electronics.

Endowed with exceptional physical and chemical properties, carbon nanotubes (CNTs) hold broad application prospects in the fields of electronics, optoelectronics, energy, composites, etc.[1–4]. In particular, horizontally aligned carbon nanotube (HACNT) arrays are considered to be one of the important candidates for constructing high-performance, low-power integrated circuits in the post-Moore era. However, the full realization of HACNT arrays has been hindered by the limitations in their fabrication process. Although numerous post-processing methods have been developed, the inevitable dispersion and arrangement of CNTs led to the introduction of damages, and impurities, and the formation of CNT bundles[5–8]. On the other hand, the direct-growth methods, known for achieving the higher purity, quality,

[1]School of Materials Science and Engineering, Peking University, Beijing, China. [2]Beijing Science and Engineering Center for Nanocarbons, Beijing National Laboratory for Molecular Sciences, College of Chemistry and Molecular Engineering, Peking University, Beijing, China. [3]State Key Laboratory of Nuclear Physics and Technology, School of Physics, Peking University, Beijing, P. R. China. [4]Key Laboratory for the Physics and Chemistry of Nanodevices and Center for Carbon-based Electronics, Department of Electronics, Peking University, Beijing, China. [5]Experimental Center of Advanced Materials School of Materials Science & Engineering, Beijing Institute of Technology, Beijing, China. [6]These authors contributed equally: Ying Xie, Yue Li, Zhisheng Peng.
✉e-mail: qianliu-cnc@pku.edu.cn; zqzhao@pku.edu.cn; jinzhang@pku.edu.cn

and better alignment, often fall short in delivering the necessary control over the uniformity, density, and size of HACNT arrays[9,10]. An innovation in HACNT-array fabrication methods is the pressing need.

Catalyst nanoparticles are pivotal in the growth of HACNT arrays. A variety of nanoparticle fabrication techniques have been established, encompassing wet chemical synthesis, mechanical milling, physical and chemical vapor deposition, as well as gas-phase processes[11]. However, in the context of achieving precise control of nanoparticle size and amount, and of mitigating nanoparticle sintering, the in-situ formation of catalysts on substrate during CNT growth is highly desired. In our previous report, we developed a Trojan catalyst method, where the catalyst precursor was spin-coated on the sapphire substrate and the catalyst elements were pre-embedded into sapphire by annealing, realizing in-situ exsolution during the CNT growth. However, the Trojan catalyst method faces challenges in maintaining its superiority in large-scale fabrication due to its reliance on traditional spin-coating approach, which struggles to achieve uniform loading of catalyst over large area and is not adept at managing the catalyst behavior in the depth-wise dimension of substrate[9]. In this regard, we identified the diminished controllability of catalyst nanoparticles as a critical gap in current fabrication methods that restricts the scalability of growing HACNT-array wafers.

By leveraging the power of ion implantation technique, featured with the horizontal uniformity beyond wafer scale and the precise controllability of the implanted ions[12–14], we introduced a shift in the preparation approach of catalyst nanoparticles, termed a nano-seeding method. Besides the catalyst pre-seeding into the sapphire substrate by ion implantation, this method also includes a substrate processing to facilitate the reconstruction of sapphire substrates, which physically confines the catalyst nanoparticles, thereby mitigating their sintering. Additionally, we designed a vertical spraying chemical vapor deposition (VSCVD) system that homogenizes gas flow and enables the uniform growth of HACNT arrays.

The exceptional control over the catalyst nanoparticles, combined with the specially designed growth equipment, enables the direct growth of wafer-scale uniform HACNT arrays. Through the nano-seeding method, a one-inch HACNT-array wafer with the highest density of 140 tubes μm^{-1} was prepared. The density distribution of the entire wafer was evaluated through an advanced high-throughput characterization technique, demonstrating good density uniformity. Furthermore, by constructing top-gate field effect transistors (FETs), we validated the excellent electronic performance of the HACNT-array wafers, with an on/off ratio approaching 10^5 and a subthreshold swing of only 134 mV dec^{-1}. Our nano-seeding method revolutionizes the preparation of catalyst nanoparticles, effectively addressing the existing challenges in the direct growth of wafer-scale uniform HACNT arrays. Moreover, this approach offers broader implications, providing insights into the construction of high-performance electronic devices.

Results and discussion

Growth of HACNT arrays through nano-seeding method

Figure 1a illustrates the schematic for the growth of HACNT arrays via the nano-seeding method. Initially, iron (Fe) ions, serving as catalyst precursors, were uniformly buried into the sapphire substrate using ion implantation technique. After annealing and subsequent hydrogen (H_2) reduction, the embedded Fe ions nucleated to form nanoparticles on the substrate surface. To further prevent nanoparticle sintering, the sapphire substrate has been reconstructed into a special strip morphology, physically confining the catalyst nanoparticles and ensuring their dispersed and active state. The implantation of catalyst elements combined with special substrate treatment constitutes the nano-seeding of catalysts, laying the foundation for the slow and uniform release of catalysts during subsequent growth process.

During the growth of HACNT-array wafer, a VSCVD system was employed to homogenize the gas flow, facilitating uniform reaction between catalysts and gaseous reactants and the uniform growth of HACNT arrays on substrates (detailed discussion in Suppl. Note 1). Figure 1b presents a photograph of the as-grown HACNT arrays on a one-inch sapphire wafer. The scanning electron microscopy (SEM) image and line mapping by Raman spectroscopy displayed in Fig. 1c demonstrate the good uniformity and high quality of the HACNT arrays (for further Raman spectra, see Suppl. Fig. 1f-h). The array densities were precisely measured using atomic force microscopy (AFM), with the highest density reaching 140 tubes μm^{-1} (Fig. 1d). The cross-sectional transmission electron microscope (TEM) images in Fig. 1e show that HACNT arrays are individual, single-walled and bundle-free. Furthermore, we used two methods to measure the alignment of arrays[5,15]. From polarized Raman spectra in Fig. 1f, we obtain that the standard deviation of the angular distribution of the HACNTs (δ) is 4.21°. The second method involved directly extracting the alignment of arrays from SEM images, which gives δ of 0.097° (Supplementary Fig. 2a, b). A comparative plot illustrating the correlation between the alignment of and the maximum density of HACNT arrays prepared by different methods was depicted in Supplementary Fig. 2c. The result demonstrates quantitatively that the nano-seeding method can achieve both superior alignment and high-density HACNT growth. A typical zoom-in SEM image in Fig. 1g strengthens the good alignment of arrays intuitively. Besides, repetitive experiments were conducted that involved the repeated growth of 1-inch HACNT-array wafers via the nano-seeding method in VSCVD system. HACNT-array wafers derived from three batches were randomly sampled and characterized. The AFM images, as shown in Supplementary Fig. 2d, show the as-grown HACNT arrays are uniformly distributed within one wafer and across different batches. The result substantiates the reproducibility of the nano-seeding method.

Unveiling the intermediate process of ion implantation

Catalysts play an important role in growing HACNT-array wafer. Unveiling the intermediate process of preparing catalysts by ion implantation is highly desirable. Time-of-flight secondary ion mass spectrometry (TOF-SIMS), featured by detecting elements at 10-ppb level and visualizing elements distribution through three-dimensional (3D) structural reconstruction at a high-resolution nanoscale, was employed[16–18]. Based on the depth profile analysis of the ion-implanted sapphire, the signal intensity of element Fe increased over time, peaking at ≈ 20 s. By converting time into depth, the distribution of Fe ions was predominantly confined within the intended depth of ≈ 3 nm within the sapphire substrate (red line in Fig. 2a). The 2D-mapping images of Fe ion intensity, extracted at increasing depths, exhibited a consistent trend (Fig. 2b). Focused ion beam (FIB) was further employed to prepare a cross-sectional sample of iron-implanted sapphire (for details see Methods). The energy-dispersive X-ray spectroscopy (EDS) mapping of iron-implanted sapphire, as shown in Fig. 2c-e, corroborates the conclusion that Fe atoms enriched in the surface of sapphire and the penetration depth was around 2–3 nm. To analyze the structure of enriched area, scanning transmission electron microscopy (STEM) was conducted. In the high-angle angular dark field (HAADF) image, different contrast of atomic columns in the surface of sapphire was observed (Fig. 2f). The specific crystallographic plane for our observation was determined to be the (0001) plane of sapphire according to the fast Fourier transform (FFT) pattern (inset in Fig. 2c). Because of the Z contrast nature of HAADF images, these high-intensity atomic columns have Fe atoms insides. This implies the substitution of Fe atoms for Al atoms in the surface of sapphire after annealing (bright dots in red circled in Fig. 2f). The intermediate process of ion implantation was further visualized by the TOF-SIMS 3D structural reconstruction of Fe and Al displayed in Fig. 2g–i. The distribution pattern of Fe ions illustrated in Fig. 2g confirmed the successful implantation of Fe ions into the predetermined depth of sapphire substrate. Figure 2h

substantiates that the homogenization of Fe ions throughout the sapphire matrix occurred after annealing.

Figuring out the intermediate process of ion implantation facilitates the regulation of growing process of HACNT arrays by designing the parameters of ion implantation. The optimal growth time (T) of HACNT arrays can be modulated by adjusting the ion energy. An increase in ion energy results in deeper implantation, thus necessitating a corresponding extension of T (Fig. 2j, Supplementary Fig. 5). Furthermore, during growth, the optimal hydrogen to carbon (H/C) ratio and the ion fluence present a negative correlation (Fig. 2k, Supplementary Fig. 6), attributable to the formation of smaller catalyst nanoparticles with smaller ion fluence. Every ion fluence corresponded to an optimal H/C ratio, except for 1×10^{16} ions cm^{-2}. Numerous big nanoparticles formed on the substrate after annealing (Supplementary Fig. 7c), which means such a fluence might exceed the solid solubility limit of Fe in Al_2O_3. As a result, carbon deposition occurred instead of CNT growth. Hence, in Fig. 2k, we represented the outlier for 1×10^{16} ions cm^{-2} with an empty square (more detailed discussions in Suppl. Note 2).

Harvesting uniform nanoparticles by substrate processing

The ion implantation facilitated the uniform pre-loading of Fe ions into the sapphire substrate. Subsequent growth of HACNT arrays necessitated the germination of embedded Fe ions and formation of dis-

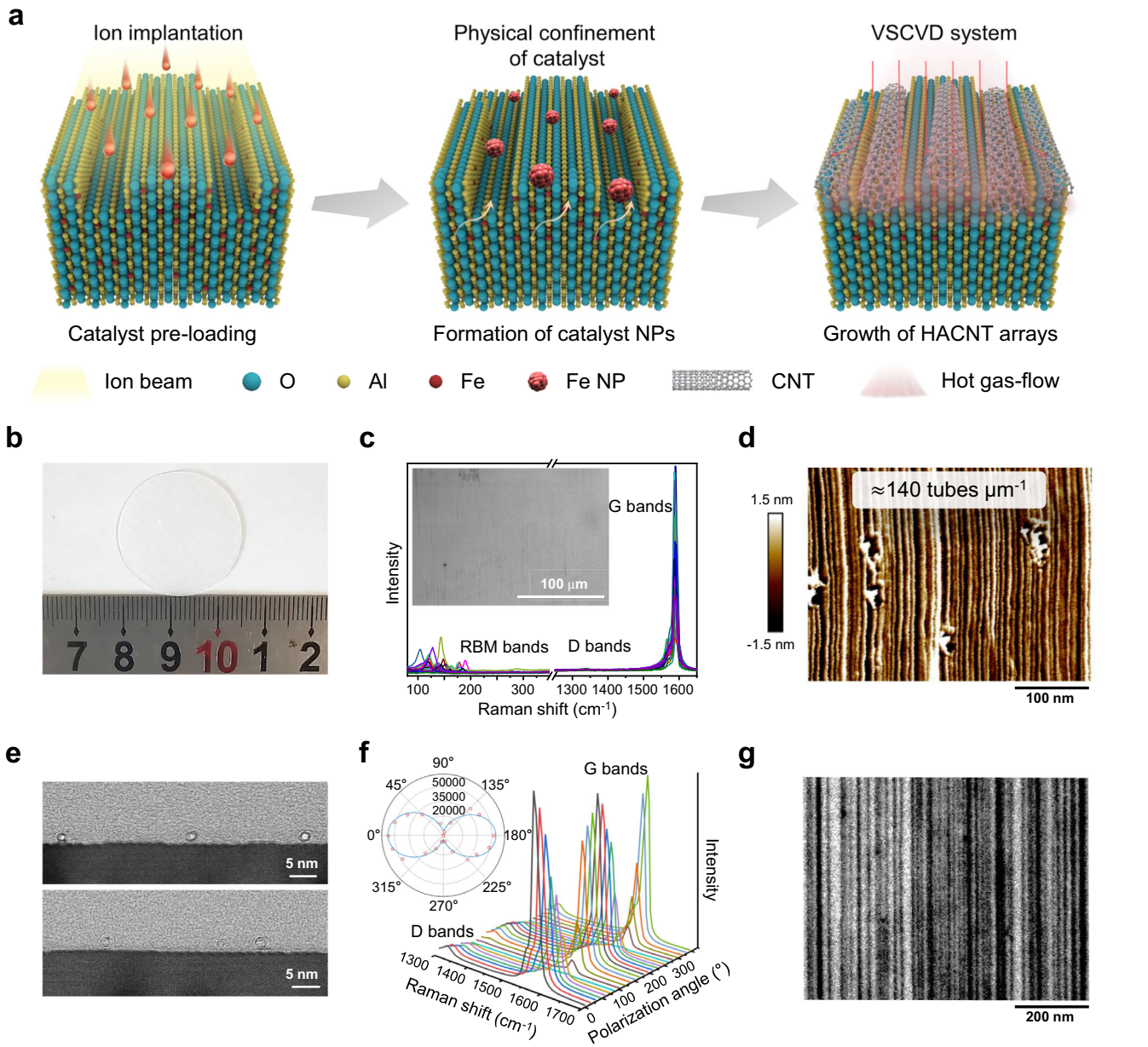

Fig. 1 | Growth of HACNT arrays through the nano-seeding method. a Schematic of the nano-seeding method: the precise loading of catalyst precursors by ion implantation, the physical confining of catalyst nanoparticles by substrate processing, and the uniform growth of HACNT arrays by VSCVD system. **b** Photograph of a one-inch HACNT-array wafer. **c** Raman line mapping spectra (at 532 nm excitation) of the arrays, inset is a typical SEM image. **d** AFM height image of the HACNT arrays showing the local highest density of 140 tubes μm^{-1}. **e** Cross-sectional TEM images of HACNT arrays. **f** Polarized Raman spectra of HACNT arrays. The polarization angle of the incident light was systematically altered by rotating a half-wave plate ($\lambda/2$) during the measurement process. Inset: Polar plot of Raman intensity as a function of polarization angle. The red dots are the measured Raman intensity of G bands. The blue line is the fitting curve. **g** Zoom-in SEM image of the HACNT arrays. Source data are provided as a Source Data file.

https://doi.org/10.1038/s41467-024-55515-0

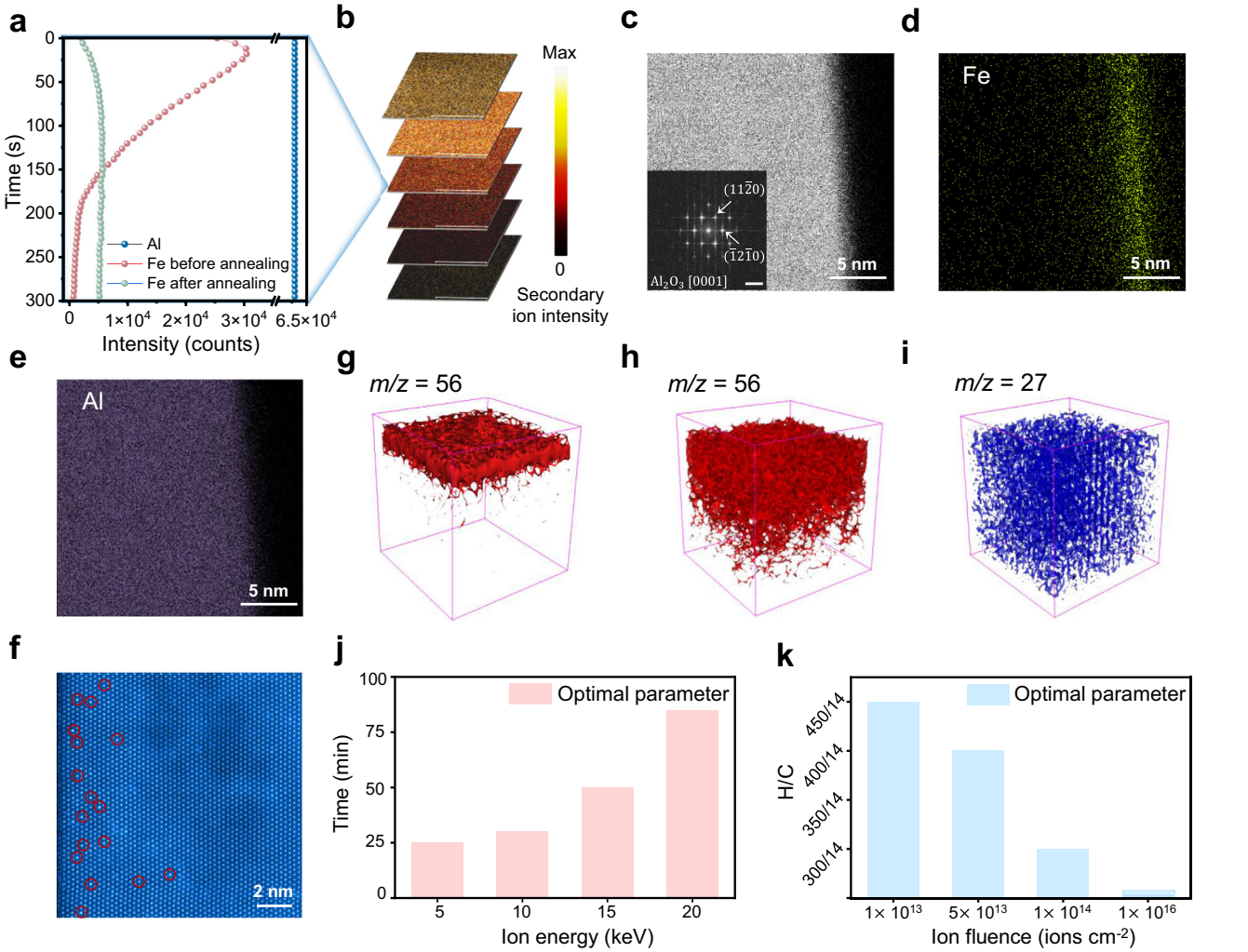

Fig. 2 | Characterization of the ion-implanted catalysts. a TOF-SIMS depth profile curves of iron-implanted sapphire before and after annealing and **b** 2D-mapping images of Fe ion intensity extracted at increasing depths, showing the variation trend of Fe ions over depth of sapphire substrate. Color scale represents the secondary ion intensity. **c**–**e** Cross-sectional STEM image **c** of an ion-implanted sapphire substrate and the corresponding EDS mappings of Fe (yellow) (**d**) and Al (purple) (**e**) elements. Inset in (**c**) is the FFT pattern of sapphire cross section (scale bar 2 nm^{-1}). **f** High magnification STEM-HAADF image demonstrated the substitution of Fe atoms for Al atoms in the surface of sapphire after annealing. **g**–**i** TOF-SIMS 3D structural reconstruction of Fe ions (red) and Al ions (blue). Fe ions concentrated in specific depth of sapphire after implantation **g** and distributed uniformly throughout the sapphire matrix after annealing (**h**). The distribution of Al ions remained after annealing (**i**). **j**–**k** Regulation of growing process of HACNT arrays by the ion energy (**j**) and the ion fluence (**k**) of ion implantation. The pink columns in **j** displayed the influence of ion energy on optimal growing time (T). The blue columns in (**k**) displayed the influence of ion fluence on optimal hydrogen to carbon (H/C) ratio. Source data are provided as a Source Data file.

persed nanoparticles on sapphire surface. To mitigate the sintering of nanoparticles, a physical confinement morphology for catalysts, created from the reconstructed sapphire substrate, was sculpted by substrate processing.

Typically, extended annealing periods lead to the reconstruction of the a-plane sapphire morphology, resulting in the formation of numerous long, thin strips on sapphire surface. These nano-scale strips act as a form of physical confinement for nanoparticles, thereby reducing their migration freedom (Fig. 3a, detailed discussion in Suppl. Note 3)[19,20]. For wafer-scale substrates, simply extending the annealing time is insufficient to achieve uniform reconstruction of surface morphology. Therefore, external forces are needed to accelerate this process, among which introducing stress can be an effective way[21]. To assist the reconstruction, we employed a facile laser-scratching process. Patterned scratches on sapphire substrate were made by a laser marking machine, which introduced uniform pre-stress on the surface (detailed discussions in Suppl. Note 4). During subsequent annealing, the release of stress accelerated the reorganization of the surface structure, leading to the formation of more and finer elongated strips. After H_2 reduction, the nanoparticles that formed on the laser-scratched sapphire substrate exhibited uniformity and narrow distribution of diameters (Fig. 3b). The introduction of pre-stress was proved by conducting Raman measurements. The observed shift in the most intense Raman peak of sapphire around 418 cm^{-1}, mapping across one scratch, confirmed the presence of higher initial stress induced by the laser-scratching method, which was found to be effective in promoting earlier crystal reconstruction (Fig. 3c)[22–25]. Raman spectra are shown in Supplementary Fig. 18.

Voronoi tessellation, a spatial analysis method, was further used to analyze the spatial distribution of nanoparticles formed on laser-scratched substrate after ion-implantation. (details in Suppl. Note 5). The variability in the areas of Thiessen polygons represents different spatial arrangement of points, which can be easily assessed by the coefficient of variation (C.V.). One of a typical Voronoi tessellation of nanoparticles prepared by the nano-seeding method was displayed in Fig. 3d (details in Supplementary Figs. 19, 20). The averaged C.V. of

https://doi.org/10.1038/s41467-024-55515-0

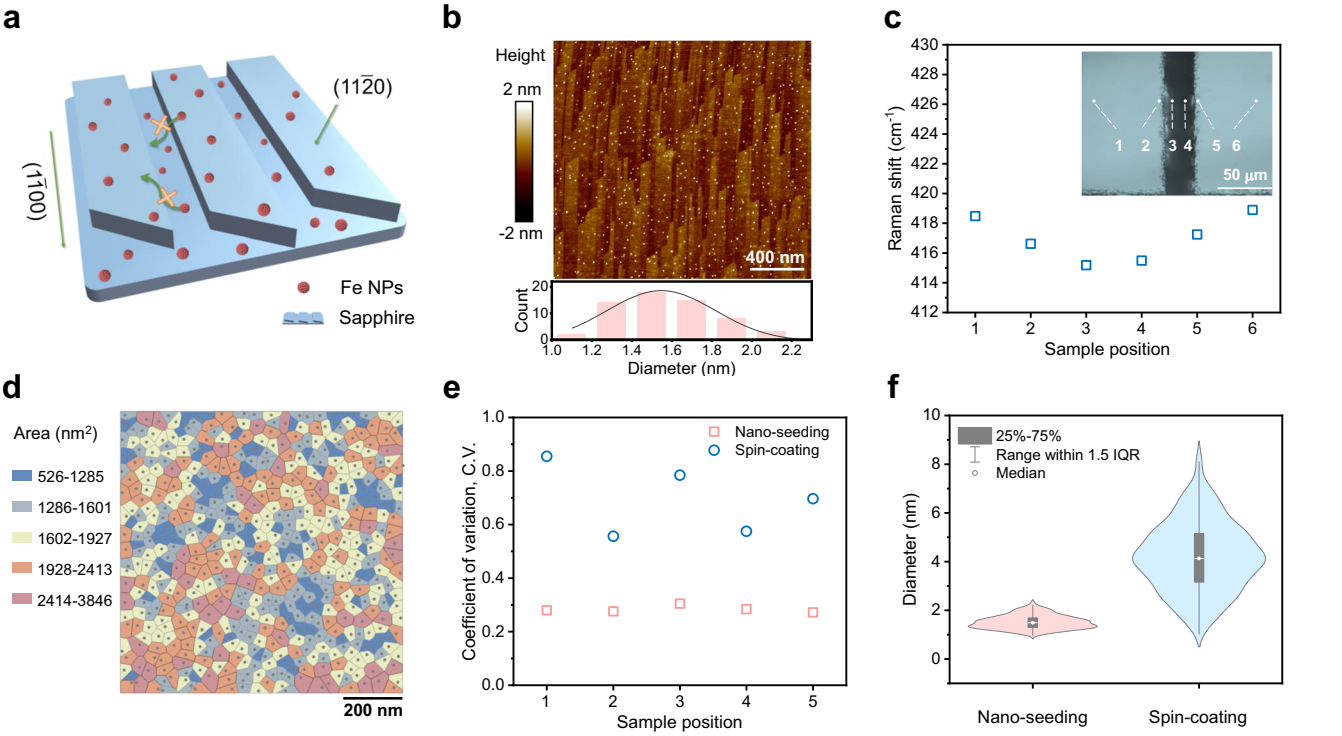

Fig. 3 | Characterization of catalyst nanoparticles prepared by the nano-seeding method. a Schematic of confining the sintering of catalyst nanoparticles on substrate by discrete a-plane strips of the reconstructed sapphire. **b** AFM image of the catalyst nanoparticles formed on the laser-scratched sapphire substrate and the histogram of diameters of nanoparticles. **c** Shifts of Raman peak of sapphire around 418 cm^{-1} when scanning across one scratch (at 532 nm excitation). Inset: optical microscopy image of one scratch. **d** A typical Voronoi tessellation of nanoparticles prepared by the nano-seeding method. Different colors represent different areas of Thiessen polygon (nm^2). (**e**) C.V. of Thiessen polygon areas of nanoparticles prepared by the nano-seeding method and spin coating method. Five regions were randomly selected from both samples. **f** Violin plots of diameters of nanoparticles prepared by the nano-seeding method and spin coating method. White lines and circles represent the median particle diameter. Dark gray boxes represent the interquartile range (IQR). Measured number of catalyst particles prepared by nano-seeding method are 584 and 602, respectively. Source data are provided as a Source Data file.

Thiessen polygon areas in nano-seeding method was 27.60% (< 33%), demonstrating the regular distribution of nanoparticles (Fig. 3e and Supplementary Table 1)[26]. Analysis of violin plots depicting nanoparticle diameters in the nano-seeding and the spin-coating method also revealed distinct characteristics (Fig. 3f and Supplementary Figs. 21–23). In the spin-coating method, the median particle diameter of 4.1 nm, delineated by white lines, and the interquartile range (IQR) of 1.99 nm, represented by dark gray boxes, indicate a larger and more dispersed distribution of nanoparticle sizes. In contrast, the broader shape of the violin plot centered around 1.5 nm in the nano-seeding method suggests a more compact and uniform particle size distribution, with a much smaller IQR of 0.39 nm. The formation of such highly dispersed small nanoparticles with uniform distribution laid a foundation for growing wafer-scale uniform HACNT arrays.

Performance portrait of HACNT-array wafer

The density uniformity of HACNT arrays was further explored. Traditional techniques for density characterization, such as AFM and TEM, while highly accurate, do not sufficiently cover the scale necessary for comprehensive wafer-level analysis. These methods are often time-consuming and limited to small, localized areas of the substrate, posing significant hurdles in high-throughput and large-area characterization[22]. To address this issue, we recently developed a technique that combines the high-throughput of polarized optical microscopy and accuracy of AFM to evaluate the density of HACNT arrays (details in Methods and Suppl. Note 7). We leveraged the AFM measurement results to bridge the functional relationship between the polarized optical images and the quantity of CNTs, thereby obtaining precise and statistically meaningful density measurement without the need to resolve individual CNTs. This technique, termed as the calibrated optical contrast (COC) method, improved characterization efficiency by 4 orders of magnitude compared to AFM measurements, making it highly suitable for evaluating the density uniformity of HACNT arrays across the wafer[27].

We used the COC technique to characterize one-inch HACNT arrays fabricated using both the nano-seeding method and the traditional method. This process began with the collection of high-throughput optical intensity data, covering the entire wafer with 576 (24 × 24) images to ensure comprehensive analysis. These images were subsequently processed to extract average optical intensity, followed by a calibration phase where AFM data from selected regions established a correlation between observed optical intensities and actual CNT densities. The calibrated data facilitated the conversion of optical intensities into detailed density mappings (Fig. 4a), allowing the density analysis of HACNT arrays across the entire wafer.

Evidently, as shown in Fig. 4b, c, the nano-seeding method yielded HACNT arrays with higher density and complete coverage of CNTs across the entire wafer (primarily ranging between 30-60 tubes μm^{-1}). In contrast, the traditional method resulted in an average density of about 10 tubes μm^{-1}, with some high-density regions (≈40 tubes μm^{-1}) and numerous uncovered areas. Through statistical distribution fitting, the density of HACNT arrays was found to meet the log-normal distribution (details in Suppl. Note 8). Here, we defined a binary descriptor: the arithmetic mean (E) of the log-normal distribution to describe the average density of HACNT arrays, and the coefficient of variation (C.V.) to evaluate the uniformity of HACNT arrays on the entire wafer. Specifically, as shown in Suppl. Table 4, the average density and the density variation of HACNT arrays were 37.18 tubes μm^{-1} and 48.62% for

https://doi.org/10.1038/s41467-024-55515-0

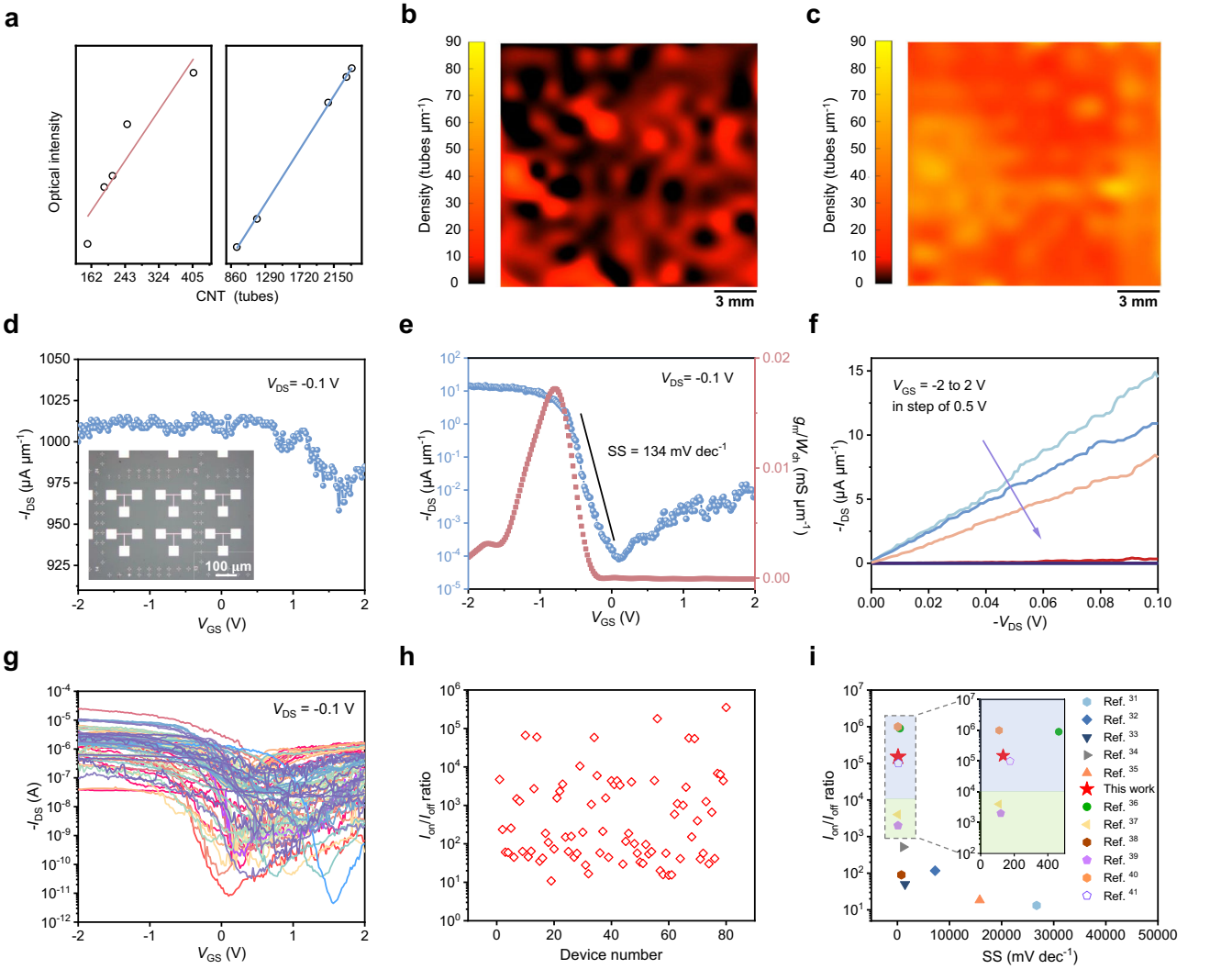

Fig. 4 | Performance portrait of HACNT-array wafer. a–c High-throughput characterization of HACNT-array density by COC technique: (**a**) Density calibration results of both the HACNT-array wafer grown by traditional method (red line) and nano-seeding method (blue line). HACNT-array density mapping of traditional wafer (**b**) and nano-seeding wafer (**c**) by COC technique. **d-i**, Electrical properties of top-gate FETs based on HACNT arrays: **d**, Transfer characteristics of a high-current device. Inset: optical microscopy image of the FETs. **e** Transfer characteristics (SS represents subthreshold swing) and (**f**) output characteristics of a typical FET device with high on/off ratio and low subthreshold swing. **g** Transfer characteristics and (**h**) on/off ratio of the measured 80 FET devices based on HACNT arrays. **i** Comparison of the on/off ratio and the subthreshold swing of HACNT-FETs prepared by the nano-seeding method against those reported in previous methods. Source data are provided as a Source Data file.

the nano-seeding method, and 8.03 tubes μm^{-1} and 107.2% for the traditional method, respectively. Apparently, the nano-seeding fabrication approach enabled a significant improvement in both the average density and the uniformity of HACNT arrays.

As a showcase of the good electrical properties, top-gate FETs with different channel lengths based on HACNT arrays were fabricated (see details in Methods). Typical devices were shown inset Fig. 4d, where the channel length (L_{ch}) is 104 nm, gate length (L_g) is 90 nm, and channel width (W) is 1 μm. We systematically measured more than 100 FET devices, including both mixed HACNT arrays and semiconducting HACNT arrays (Fig. 4d–h). Experiments revealed that mixed HACNT arrays exhibit excellent electrical conductivity, with on-state current exceeding 1000 μA μm^{-1} at a drain bias of -0.1 V (Fig. 4d), much higher than in refs. 9,28–30. The FET devices based on semiconducting HACNT arrays displayed a subthreshold swing (SS) of only 134 mV dec^{-1} and an on/off ratio approaching 10^5. The transconductance reached up to 0.02 mS μm^{-1} at bias voltage V_{DS} = −0.1 V (Fig. 4e). Output characteristics of the FETs with V_{GS} varying from −2 to 2 V in step of 0.5 V was shown in Fig. 4f. 80 FET devices based on semiconducting HACNTs were measured for a more comprehensive analysis of the electrical properties. The transfer characteristics and the on/off ratio are plotted in Fig. 4g, h, respectively. Among them, the proportion of FETs with on/off ratio exceeding 10^4 is greater than 10%. Comparison of the key electrical parameters-namely, the on/off current ratio and subthreshold swing-of the HACNT arrays prepared by the nano-seeding method was conducted against those reported in previous methods. The comparative analysis is graphically depicted in Fig. 4i[31–41]. In comparison, our HACNT arrays show obvious advantages in high switching ratio of 10^5 and low subthreshold swing of 134 mV dec^{-1}, which is among the top in terms of FET performance. As mentioned above, the electrical properties of HACNT arrays prepared by the nano-seeding method have been testified, highlighting their great potential for application in ICs.

In summary, to address the pressing need for innovation in HACNT-array fabrication, we presented a nano-seeding method that enables uniform and controllable preparation of catalyst nanoparticles and direct growth of high-density, wafer-scale uniform HACNT arrays. This method transcended the traditional limitations of HACNT-array

fabrication, offering an approach that improves the uniformity, density, and size of HACNT arrays significantly. The integration of ion implantation technique with substrate processing has revolutionized the preparation of catalyst nanoparticles. The introduction of the VSCVD system has been instrumental in achieving homogeneous gas flow and uniform interaction between reactants and catalysts across the wafer scale.

The fabrication of one-inch HACNT-array wafers with a highest density of 140 tubes μm^{-1} stands as a testament to the efficacy of our nano-seeding method. Employing the advanced high-throughput characterization technique, we confirmed the good uniformity of HACNT-array wafers. FETs based on such HACNT arrays further validated their exceptional electrical performances and potential for application in carbon-based ICs. The scalability and control of HACNT arrays offered by our nano-seeding method represents a leap forward in the direct growth of HACNT arrays, which heralds possibilities in full-scale integration of HACNT arrays into practical applications.

Methods

Preparation of catalysts by ion implantation technique

The Fe ion implantation was conducted at room temperature (RT) by employing a home-built ion implanter (FM-400) at Beijing Radiation Center. The ion fluence was set as 1×10^{13}, 5×10^{13}, 1×10^{14}, and 1×10^{16} ions cm^{-2}. The ion energy was set as 5, 10, 15, and 20 keV. The stopping and range of ions in matter (SRIM) computer program was used to study the physical process of ion implantation. Specifically, the transport of ions in matter (TRIM) was employed to simulate the interactions of energetic Fe ions with sapphire substrates by Monte Carlo method. Fe concentration versus implantation depth was subsequently calculated. After ion implantation, another annealing process at 1100 °C in air for 8 h was conducted to repair the radiation damage of the substrate surface.

Creating physical confinement by substrate processing

The a-plane $(11\bar{2}0)$ sapphire substrates sized from 4×6 mm^2 to one-inch (single-side polished, miscut angle < 0.5°, surface roughness < 0.5 nm) were purchased from Hefei Kejing Materials Technology Co., China. Before cleaning, the laser marking machine (HGTECH LSU3EA, 24 w, 355 nm) was used to make patterned scratches on the substrate, forming a grid of squares with different size, ranging from 1×1 mm^2, 2×2 mm^2, to 4×4 mm^2. The laser processing cycles varied from 1, 50, 100, to 200 times. Other parameters kept fixed: the frequency was set at 100 kHz, the *Q* pulse width was 0.1 s, and the speed was 20 mm s^{-1}. Thereafter, the substrates processed by laser scratching as well as the normal substrates without laser processing were all subjected to the ultrasonic cleaning in Milli-Q water, followed by acetone, ethanol, and Milli-Q water again for 10 min, respectively. Then, these sapphire substrates underwent an annealing process at 1100 °C in air for different times (from 8 to 48 h).

Design of the VSCVD system

The VSCVD system was composed of gas flow system, vacuum system, electric control system, gas mixing system, spraying system, growth system, and sample injection system. Before getting into the reactor, all the reactant gases were pre-mixed uniformly in a mixing tank. After that they passed through the furnace which consisted of two heating zones. The upper one set at lower temperature was used to pre-heat the gases, and the bottom one with higher temperature was used to grow HACNT arrays. Here, the gas mixture was sprayed uniformly onto the substrate by a quartz spray unit for the growth of HACNT arrays. The spraying distance can be precisely regulated by an adjustable sample rod.

Growth of HACNT arrays by nano-seeding method

The growth of wafer-scale high-density HACNT arrays by the nano-seeding method was as following: the laser scratched sapphire substrate loaded with ion implanted Fe catalyst precursors was transferred into the specially designed VSCVD reactor furnace that operated at a set temperature of 830 °C under 70 kPa. When heated to the set temperature, the system was vacuumized to 20 Pa, then purged with 1000 cm^3 STP min^{-1} argon to atmospheric pressure. Such a cleaning program was repeated for two times to exhaust the air. Then the growing program began: First, 300 cm^3 STP min^{-1} argon and 300 cm^3 STP min^{-1} hydrogen were introduced for 3 min to reduce the Fe ions from the substrate and form Fe nanoparticles in-situ. Afterwards, another flow of 14 cm^3 STP min^{-1} argon was introduced through an ethanol bubbler as carbon feedstock for the growth of HACNT arrays. During growth, the argon kept fixed in 300 cm^3 STP min^{-1}, while the hydron varied from 300 cm^3 STP min^{-1} to 500 cm^3 STP min^{-1}. All gas flows into the reactor were controlled using mass flow controllers (MFCs). The pressure was kept at 70 kPa through the entire growth process. The spraying distance was set as 10 mm.

Growth of HACNT arrays by traditional method

To demonstrate the superiority of the nano-seeding method, for comparison, we also grew HACNT arrays in a horizontal furnace, and the catalyst precursor was spin-coated on the sapphire substrate that was not processed by laser-scratching before annealing. The specific growing procedure was as following: First, the a-plane sapphire substrate underwent annealing at 1100 °C in air for 16 h. Then, we prepared the $Fe(OH)_3$ colloid by dropping $FeCl_3$ solution into boiled water. The $Fe(OH)_3$ colloid was diluted by ethanol to 0.05 mmol L^{-1} and was spin-coated on sapphire surface. The growth of HACNT arrays was conducted in a horizontal reactor furnace operated at a set temperature of 830 °C. When heated in air to set temperature, the system was purged with 300 cm^3 STP min^{-1} argon for 10 min, followed by a flow of 300 cm^3 STP min^{-1} hydrogen for 7 min. Afterwards, another flow of 80 cm^3 STP min^{-1} argon was introduced through an ethanol bubbler for the growth of HACNT arrays. All gas flows into the reactor were controlled using mass flow controllers (MFCs). Such a method of preparing HACNT arrays was termed as a "traditional method" in the main text.

General characterization

SEM images were obtained on a Hitachi S4800 SEM operated at 1.0 and 10 kV. Raman spectra of SWNTs with line mapping conducted with a scan step of 5 μm and a laser beam spot of 1 μm was collected from Jovin Yvon-Horiba LabRam systems with 532 nm excitation. As for demonstrating the tensile strain introduced by laser scratching, the point-by-point scanning across the scratch was conducted with 532 nm excitation. AFM images were obtained using a Dimension Icon microscope (Bruker).

TOF-SIMS measurements were conducted with a PHI nano TOF II (ULVAC-PHI Inc., Japan). A Bi_3^{++} (a small cluster of three Bi atoms with two charges) beam (30 kV) was used as the primary beam to detect the samples, and the sputter etching was performed using an Ar^+ beam (3 kV 100 nA) to obtain the desired depth profile. The area of analysis was 20×20 μm^2, while the sputtering area was 400×400 μm^2.

Cross section-TEM sample was prepared by focused ion beam methods (FIB, using a TESCAN Solaris FIB dual beam SEM). To avoid the damage of ion beam, the sample was coated by a thick layer of carbon. Then, trenching milling was performed initially at 20 nA and then at 10 nA and 2.5 nA for polishing until a trench was prepared. Then a lamella sample was cut (U-cut) and transferred to copper grids. Next, the lamella was first polished by ion beam at 250 and 150 pA under 30 kV until its thickness is less than 200 nm. Finally, lamella was polishing to < 50 nm thick by ion beam at 20 pA under 2 kV with over and under tilting below 2°. Cross-section scanning transmission electron microscopy characterization was performed by using a JEM-ARM300F2 GRAND ARM™2 atomic resolution electron microscopy equipped with double aberration correction system. HAADF images (collection angle: 80–180 mrad) and EDS spectra was acquired during TEM characterization.

Polarized Raman spectroscopy was conducted by rotating the polarizer between 0–360° and recording a series of Raman spectra to extract the relationship between the G-peak intensity and the polarization direction. From the maximum and minimum intensity values, the standard deviation of the angular distribution of the CNTs were determined. Directly extracting the alignment of HACNT arrays from SEM images was conducted by measuring the angle θ between each CNT and the vertical direction, and calculating the standard deviation δ from the statistical results.

High-throughput density characterization of HACNT wafers

The COC technique was utilized for high-throughput density characterization of HACNT wafers. Due to the strong depolarization effect of CNTs, excellent optical contrast can be achieved under specific polarization settings. Moreover, a simple linear relationship exists between CNTs and optical reflectance. With proper calibration, this allows for high-throughput and accurate quantitative density measurements. Specifically, the optical characterization setup involves a Nikon Eclipse LV100N POL microscope equipped with objectives ranging from 10× (N.A. = 0.3) to 100× (N.A. = 0.9) for varying levels of magnification. Polarized optical images are captured using two polarizers (Nikon LV-PO), where the first polarizer (P_1) is placed in the incident beam and the second (P_2) in the reflective beam, with the ability to rotate the latter with a precision of 0.1°. Specifically, δ is around ±6° in this work. Illumination is provided by a Nikon LV-LH50PC halogen lamp. Aperture and field iris diaphragms are used to control the beam, minimizing excess light. For birefringent substrates, refractive index matching is employed to reduce unwanted reflections. The typical image exposure time was 1.0 s. During sample mapping, optical images are taken uniformly across a 24 × 24 grid on the entire wafer sample, and the optical signal is converted into density using a calibration function to obtain a density mapping of the entire wafer sample. The accuracy of this method has been validated against high-resolution techniques such as AFM and SEM, ensuring reliable and consistent CNT characterization[42].

Fabrication and measurements of electrical devices

Top-gated FET devices were fabricated by the following steps: (1) Marks for alignment were first patterned on the substrate by electron beam lithography (EBL). Then Ti/Pd film of 10/70 nm thickness was deposited by electron beam evaporation (EBE) and a lift-off process was followed. (2) The channel area was defined by EBL and redundant CNTs were removed by reaction ion etching (RIE) with 60 cm^3 STP min^{-1} oxygen flow and 80 W ratio frequency generator power for 30 s. (3) Source and drain contacts, along with test pads connected to source and drain, were patterned by EBL, and deposited of Pd film of 70 nm thickness by physical vapor deposition (PVD). A lift-off process was followed. (4) Y was deposited for a 0.6 nm thickness to improve the HfO_2 growth on the CNT-array-covered substrate. After that, HfO_2 film of 5 nm thickness was deposited by atomic layer deposition (ALD). (5) Gate electrode and test pad connected to it were patterned by EBL, and deposited of Pd film of 70 nm thickness by EBE. A lift-off process was followed. For measurement of electrical devices, an Agilent B1500A Semiconductor Device Analyzer and a probe station (EPS) were used to perform electrical characterizations at room temperature under ambient conditions.

Reporting summary

Further information on research design is available in the Nature Portfolio Reporting Summary linked to this article.

Data availability

The data that support the findings of this study are available from the corresponding authors upon request. Source data are provided with this paper.

Code availability

The codes that support the findings of this study are available from the corresponding authors upon request.

References

1. Behabtu, N. et al. Strong, light, multifunctional fibers of carbon nanotubes with ultrahigh conductivity. *Science* **339**, 182–186 (2013).
2. Franklin, A. D. Electronics: the road to carbon nanotube transistors. *Nature* **498**, 443–444 (2013).
3. Aasmundtveit, K. E., Roy, A. & Ta, B. Q. Carbon nanotubes directly integrated in CMOS by local synthesis towards a wafer-level process. *Ieee Nanotechnol. Mat*, 121–125https://doi.org/10.1109/NMDC.2018.8605926 (2018).
4. Hills, G. et al. Modern microprocessor built from complementary carbon nanotube transistors. *Nature* **572**, 595–602 (2019).
5. Liu, L. et al. Aligned, high-density semiconducting carbon nanotube arrays for high-performance electronics. *Science* **368**, 850–856 (2020).
6. Sun, W. et al. Precise pitch-scaling of carbon nanotube arrays within three-dimensional DNA nanotrenches. *Science* **368**, 874–877 (2020).
7. He, X. et al. Wafer-scale monodomain films of spontaneously aligned single-walled carbon nanotubes. *Nat. Nanotechnol.* **11**, 633–638 (2016).
8. Jinkins, K. R. et al. Aligned 2D carbon nanotube liquid crystals for wafer-scale electronics. *Sci. Adv.* **7**, eabh0640 (2021).
9. Hu, Y. et al. Growth of high-density horizontally aligned SWNT arrays using Trojan catalysts. *Nat. Commun.* **6**, 6099 (2015).
10. Xie, Y. et al. Growth of homogeneous high-density horizontal SWNT arrays on sapphire through a magnesium-assisted catalyst anchoring strategy. *Angew. Chem. Int. Ed.* **60**, 9330–9333 (2021).
11. Azam, M. A., Zulkapli, N. N., Nawi, Z. M. & Azren, N. M. Systematic review of catalyst nanoparticles synthesized by solution process: towards efficient carbon nanotube growth. *J. Sol. -Gel. Sci. Techn.* **73**, 484–500 (2015).
12. Wang, G. et al. Seamless lateral graphene p-n junctions formed by selective in situ doping for high-performance photodetectors. *Nat. Commun.* **9**, 5168 (2018).
13. Zhao, Y. et al. Ion implantation assisted synthesis of graphene on various dielectric substrates. *Nano Res.* **14**, 1280–1286 (2020).
14. Bangert, U. et al. Ion implantation of graphene-toward IC compatible technologies. *Nano Lett.* **13**, 4902–4907 (2013).
15. Guo, Y. et al. Soft-lock drawing of super-aligned carbon nanotube bundles for nanometre electrical contacts. *Nat. Nanotechnol.* **17**, 278–284 (2022).
16. Sodhi, R. N. Time-of-flight secondary ion mass spectrometry (TOF-SIMS):-versatility in chemical and imaging surface analysis. *Analyst* **129**, 483–487 (2004).
17. Yang, L. et al. Depth profiling and melting of nanoparticles in secondary ion mass spectrometry (SIMS). *J. Phys. Chem. C.* **117**, 16042–16052 (2013).
18. Song, T. L. et al. Probing surface information of alloy by time of flight-secondary ion mass spectrometer. *Crystals* **11**, 1465 (2021).
19. Hu, Y. et al. Confined Fe catalysts for high-density SWNT arrays growth: a new territory for catalyst-substrate interaction engineering. *Small* **17**, e2103433 (2021).
20. Simeonov, K. & Lederman, D. Surface structure of $(11\bar{2}0)$ Al_2O_3 single crystals after high temperature annealing. *Surf. Sci.* **603**, 232–236 (2009).
21. Xie, X. et al. Microwave purification of large-area horizontally aligned arrays of single-walled carbon nanotubes. *Nat. Commun.* **5**, 5332 (2014).
22. Xie, Y., Li, Y., Zhao, Z. Q. & Zhang, J. Pave the way to the batch production of SWNT arrays for carbon-based electronic devices. *Nano Res.* **16**, 12516–12530 (2023).

23. Gurarie, V. N., Otsuka, P. H., Jamieson, D. N. & Prawer, S. Raman-based analysis of implantation-induced expansion and stresses in sapphire crystals. *J. Mater. Res.* **20**, 1131–1138 (2005).
24. Wermelinger, T., Borgia, C., Solenthaler, C. & Spolenak, R. 3-D Raman spectroscopy measurements of the symmetry of residual stress fields in plastically deformed sapphire crystals. *Acta Mater.* **55**, 4657–4665 (2007).
25. Jia, W. & Yen, W. M. Raman-Scattering from Sapphire Fibers. *J. Raman Spectrosc.* **20**, 785–788 (1989).
26. Duyckaerts, C. & Godefroy, G. Voronoi tessellation to study the numerical density and the spatial distribution of neurones. *J. Chem. Neuroanat.* **20**, 83–92 (2000).
27. Benedict, L. X., Louie, S. G. & Cohen, M. L. Static polarizabilities of single-wall carbon nanotubes. *Phys. Rev. B Condens Matter* **52**, 8541–8549 (1995).
28. He, M., Zhang, S. & Zhang, J. Horizontal single-walled carbon nanotube arrays: controlled synthesis, characterizations, and applications. *Chem. Rev.* **120**, 12592–12684 (2020).
29. Kang, L. X. et al. Large-area growth of ultra-high-density single-walled carbon nanotube arrays on sapphire surface. *Nano Res.* **8**, 3694–3703 (2015).
30. Wang, C. A. et al. Synthesis and device applications of high-density aligned carbon nanotubes using low-pressure chemical vapor deposition and stacked multiple transfer. *Nano Res.* **3**, 831–842 (2010).
31. Zhang, S. et al. Selective scission of C-O and C-C bonds in ethanol using bimetal catalysts for the preferential growth of semiconducting SWNT arrays. *J. Am. Chem. Soc.* **137**, 1012–1015 (2015).
32. Kang, L. et al. Growth of close-packed semiconducting single-walled carbon nanotube arrays using oxygen-deficient TiO_2 nanoparticles as catalysts. *Nano Lett.* **15**, 403–409 (2015).
33. Kang, L., Zhang, S., Li, Q. & Zhang, J. Growth of horizontal semiconducting SWNT arrays with density higher than 100 tubes/μm using ethanol/methane chemical vapor deposition. *J. Am. Chem. Soc.* **138**, 6727–6730 (2016).
34. Liu, B. et al. Nearly exclusive growth of small diameter semiconducting single-wall carbon nanotubes from organic chemistry synthetic end-cap molecules. *Nano Lett.* **15**, 586–595 (2015).
35. Qin, X. et al. Growth of semiconducting single-walled carbon nanotubes by using ceria as catalyst supports. *Nano Lett.* **14**, 512–517 (2014).
36. Wang, J. T. et al. Growing highly pure semiconducting carbon nanotubes by electrotwisting the helicity. *Nat. Catal.* **1**, 326–331 (2018).
37. Bishop, M. D. et al. Fabrication of carbon nanotube field-effect transistors in commercial silicon manufacturing facilities. *Nat. Electron.* **3**, 492–501 (2020).
38. Cao, Y. et al. Radio frequency transistors using aligned semiconducting carbon nanotubes with current-gain cutoff frequency and maximum oscillation frequency simultaneously greater than 70 GHz. *ACS Nano* **10**, 6782–6790 (2016).
39. Si, J. et al. A carbon-nanotube-based tensor processing unit. *Nat. Electron.* **7**, 684–693 (2024).
40. Cheng, X. et al. Aligned carbon nanotube-based electronics on glass wafer. *Sci. Adv.* **10**, eadl1636 (2024).
41. Lin, Y. X. et al. Scaling aligned carbon nanotube transistors to a sub –10 nm node. *Nat. Electron.* **6**, 506–515 (2023).
42. Li, Y. et al. Calibrated absolute optical contrast for high-throughput characterization of horizontally aligned carbon nanotube arrays. *Nano Today* **59**, 102502 (2024).

Acknowledgements

J.Z. acknowledges the financial support from the National Key R&D Program of China (2022YFA1203302), the National Natural Science Foundation of China (52021006), the Strategic Priority Research Program of CAS (XDB36030100), the Beijing National Laboratory for Molecular Sciences (BNLMS-CXTD-202001) and the Shenzhen Science and Technology Innovation Commission (KQTD20221101115627004). L.Q. acknowledges funding from the National Key R&D Program of China (2022YFA1203304) and the National Natural Science Foundation of China (52102032). Z.Z. acknowledges funding from the National Natural Science Foundation of China (52272033). X.Z thanks support from the National Key R&D Program of China (2024YFE0109200). Z.P acknowledges support from the Postdoctoral Fellowship Program of CPSF (GZC20230034) and the China Postdoctoral Science Foundation (2024M750091). The authors thank Prof. Chuanhong Jin and Huimin Yin from Zhejiang University for their technical supports in preparing the cross-sectional TEM samples by FIB methods.

Author contributions

Y.X. and Y.L. prepared the samples and performed the experiments of growing and characterizing HACNT arrays. C.W. and Z.P., supervised by J.S., performed the fabrication and measurement of CNT-FETs. Z.Q. and X.C., supervised by X.Z., conducted the STEM-HAADF characterization and the corresponding data analysis. T.S. conducted TOF-SIMS measurement, and helped to analyze the data. Y.X., Y.L. and L.Q. wrote and revised the manuscript with input from all authors. J.Z., L.Q. and Z.Z. supervised the overall projects. All authors contributed to the discussion and writing of this manuscript.

Competing interests

The authors declare no competing interests.

Additional information

Supplementary information The online version contains supplementary material available at https://doi.org/10.1038/s41467-024-55515-0.

Correspondence and requests for materials should be addressed to Liu Qian, Ziqiang Zhao or Jin Zhang.

Peer review information *Nature Communications* thanks the anonymous reviewers for their contribution to the peer review of this work. A peer review file is available.